Mysen *Progress in Earth and Planetary Science* (2018) 5:6
DOI 10.1186/s40645-017-0161-6

Progress in Earth and Planetary Science

RESEARCH ARTICLE Open Access

Mass transfer in the Earth's interior: fluid-melt interaction in aluminosilicate–C–O–H–N systems at high pressure and temperature under oxidizing conditions

Bjorn Mysen

Abstract

Understanding what governs the speciation in the C–O–H–N system aids our knowledge of how volatiles affect mass transfer processes in the Earth's interior. Experiments with aluminosilicate melt + C–O–H–N volatiles were, therefore, carried out with Raman and infrared spectroscopy to 800 °C and near 700 MPa in situ in hydrothermal diamond anvil cells. The measurements were conducted in situ with the samples at the desired temperatures and pressures in order to avoid possible structural and compositional changes resulting from quenching to ambient conditions prior to analysis. Experiments were conducted without any reducing agent and with volatiles added as H_2O, CO_2, and N_2 because both carbon and nitrogen can occur in different oxidation states.

Volatiles dissolved in melt comprise H_2O, CO_3^{2-}, HCO_3^-, and molecular N_2, whereas in the coexisting fluid, the species are H_2O, CO_2, CO_3^{2-}, and N_2. The HCO_3^-/CO_3^{2-} equilibrium in melts shift toward CO_3^{2-} groups with increasing temperature with $\Delta H = 114 \pm 22$ kJ/mol. In fluids, the CO_2 abundance is essentially invariant with temperature and pressure. For fluid/melt partitioning, those of H_2O and N_2 are greater than 1 with temperature-dependence that yields ΔH values of -6.5 ± 1.5 and -19.6 ± 3.7 kJ/mol, respectively. Carbonate groups, CO_3^{2-} are favored by melt over fluid. Where redox conditions in the Earth's interior exceed that near the QFM oxygen buffer (between NNO and MW buffers), N_2 is the stable nitrogen species and as such acts as a diluent of both fluids and melts. For fluids, this lower silicate solubility, in turn, enhances alkalinity. This means that in such environments, the transport of components such as high field strength cations, will be enhanced. Effects of dissolved N_2 on melt structure are considerably less than on fluid structure.

Keywords: Volatiles, Spectroscopy, Melt structure, Fluid structure, Temperature, Pressure

Introduction

Characterization of the processes that govern the budget and recycling of volatile components in the Earth's interior is central to our understanding of the formation and evolution of the solid Earth, its oceans, and atmosphere (e.g., Kasting et al. 1993; Jambon 1994; Tolstikhin and Marty 1998; Deines 2002). However, our knowledge of the nitrogen abundance in the Earth's mantle and in mantle-derived magma is not well established with model-dependent mantle abundance suggested between about 1 and 35 ppm (Marty, 1995; Javoy, 1997). The nitrogen abundance likely also is heterogeneously distributed with considerably greater nitrogen contents in subduction zone environments where abundances above 0.1% N_2 have been reported (Fisher et al. 2002). This latter environment likely also is where most of the exchange of volatiles (including nitrogen) occurs between the solid Earth and the atmosphere (Schmidt and Poli, 2003; Bebout, 2007).

Transfer of nitrogen from the Earth's interior to the surface and atmosphere is accomplished via partitioning of nitrogen between solid mantle, partial melts and perhaps multicomponent fluids with melt/mineral and fluid/mineral N_2 partition coefficients exceeding 1. Mass transport is at the core of these processes.

Correspondence: bmysen@carnegiescience.edu
Geophysical Laboratory, Carnegie Instn. Washington, Washington DC, USA

Characterization of transport processes requires data and models that describe physico-chemical properties of silicate melts and C–O–H–N fluids at high temperature and pressure under controlled redox conditions. Redox conditions are important because even within the redox range of natural magmatic processes in the Earth's interior (Carmichael and Ghiorso 1990; Wood et al. 1990), carbon and nitrogen, in particular, may occur in different oxidation states (Libourel et al. 2003; Kadik et al. 2004 2010; Mysen et al. 2008 Mysen et al. 2011; Li and Keppler 2014). The nitrogen solubility and solution mechanism(s) in silicate melts are sensitive to the redox state of nitrogen (Libourel et al., 2003; Mysen and Yamashita, 2010; Kadik et al. 2015) and needs to be controlled, therefore, during experiments in order to describe the behavior of nitrogen during melting and crystallization in the Earth's interior.

Nitrogen is but one of several volatile components in the Earth's interior with the system C–O–H–N comprising the main components (Jambon, 1994). Solubility and solution mechanisms of C–O–H–N components in silicate melts and of silicate components in C–O–H–N fluid are, therefore, necessary, and may be carried out experimentally (e.g., Franz 1998; Newton and Manning 2005 2006; Li and Keppler 2014; Kadik et al. 2015). However, most of that information is from analysis of glasses formed by temperature-quenching of volatile-containing melts to form a glass at ambient temperature at high pressure followed by decompression and, finally, examination of these glasses. Application of such data to characterize high-temperature/pressure melts and fluids relies on the assumption that there are no changes of these materials as they are brought from high temperature and high pressure to ambient conditions. The structure of a glass formed is this way is not that of the melt. Rather, it is the structure frozen in at the glass transition (e.g., Moynihan et al. 1976; Richet and Bottinga 1986; Dingwell and Webb 1990; Richet et al. 1992) because melt structure is temperature (and pressure) dependent (e.g., Stebbins 1988; Mysen et al. 2003; Agee 2008; Yamada et al. 2011; Wu et al. 2014). Moreover, in melts that contain volatiles, their speciation can be temperature- and pressure-dependent (Nowak and Behrens, 1995; Mysen and Yamashita 2010; Wu et al. 2014). In addition, during quenching to ambient temperature and pressure, some or all of the volatiles may exsolve from the cooling melt because the solubility of volatiles in melts varies with both temperature and pressure. Therefore, neither the volatile content nor the speciation of a glass is that which existed in its molten state at high temperature and pressure.

An additional problem associated with examination of quenched material as a proxy of high-temperature/pressure is that the structure of C–O–H–N fluids in equilibrium with silicate at high temperature and pressure cannot be quenched for quantitative structure study at ambient conditions. This is partly because silicate and other oxides dissolved in fluids at such high temperatures and pressures often precipitate during quenching (e.g., Zhang and Frantz 2000; Mysen and Armstrong 2002; Kessel et al. 2004), and partly because the C–O–H–N fluid structure may change as pressure and temperature are reduced from the experimental to ambient conditions (e.g., Mysen and Yamashita 2010; Wu et al. 2014). In summary, it is necessary, therefore, to study melts and fluids at the temperature and pressure of interest in order to attain quantitative understanding of their structure and their structure-property relations.

Recent experimental studies have addressed structural and compositional aspects of silicate–COH fluid + melt systems while samples were at high temperature and pressure (Ni and Keppler 2013; Mysen 2015a, b). Less is known about chemically more complex situation in which the C–O–H–N system of volatiles in equilibrium with aluminosilicate melts. The objective of the present study is to address this latter type of system in order to provide experimental data with which to further our understanding the structure of fluids and melts of aluminosilicate–C–O–H–N systems relevant in the temperature and pressure range of the Earth's crust and upper mantle under oxidizing conditions.

The experiments were conducted under conditions where nitrogen exists in its oxidized state, N_2. We note, though, that nitrogen may be reduced to amide and ammine forms at and above hydrogen fugacities between those defined by the NNO–H_2O (nickel–nickel oxide) and MW–H_2O (magnetite–wüstite) redox conditions (Mysen et al. 2008), which are redox conditions within the range encountered in the Earth's interior (Wood et al. 1990; Frost and McCammon, 2008). This information is, therefore, relevant only to the most oxidized part of this range of redox conditions.

Methods/Experimental

Optical and vibrational spectroscopic data from the samples were recorded while these were at the desired high pressure and temperature while contained in externally heated, hydrothermal diamond anvil cells (HDAC) of the type originally described by Bassett et al. (1996). In this cell, the upper and lower diamonds are surrounded by Mo wrap-around wire heaters. Two thermocouples in contact with the upper and lower diamonds, respectively, are located within less than 1 mm from the sample. The samples, themselves, were contained in the cell within 125 μm thick Ir gaskets with a 500 μm diameter sample hole. Iridium was used as gasket material because it does not react with the sample (melt and fluid) at the temperature and pressure conditions of these experiments.

The temperature was measured with K-type thermocouples that were calibrated against the melting temperature of NaCl (800.5 °C). Temperature error was about ± 3 °C with the thermal gradient across the sample volume less than 2 °C. Pressure was generated by the fluid at high temperature in the cell. Pressure is, therefore, a dependent variable in these experiments. It was determined from the one-phonon Raman shift of ^{13}C synthetic diamond, which was used to avoid interference with the Raman signals of ^{12}C from the diamond cell itself (Bassett et al. 1996; Schiferl et al. 1997; Mysen and Yamashita 2010). Ten to 30 μm across diamond pieces were grown from $^{13}CH_4$ by using CVD techniques (Liang et al. 2009). Pressure uncertainty at high temperature is ± 110 MPa and precision ± 40 MPa determined from the precision of the Raman spectrometer (± 0.1 cm^{-1} by using Ne lines as internal spectrometer calibrant) and the uncertainty in the calibration by Mysen and Yamashita (2010).

The samples in the diamond cell were examined through optical microscopy and via confocal micro-Raman and microFTIR methods while at the temperature and pressure of interest. In the Raman spectroscopic studies, the samples (melt and fluid) were excited with the 490 nm line of a solid state laser in a JASCO model NRS-3100 confocal micro-Raman spectrometer. The spectrometer is equipped with a single monochromator, a holographic notch filter, and holographic gratings with 600, 1200, and 2400 grooves/mm. The laser was focused to about 1 μm diameter at the sample with power at the sample typically near 30 mW. Spectra were recorded through a × 50 magnification/0.42 N.A. long-working distance Mitutoyo objective lens. An Andor Model DV401-F1 1024 × 128 pixel (25 μm pixel size) Peltier-cooled CCD was used for signal detection. By using the confocal optics, > 85% of the signal was recorded from within 30 μm of a sample surface (Mysen 2015a). For infrared spectroscopy, a JASCO model IMV4000 FTIR microscope system operating in transmission mode with 10X objective and condenser cassegrain lenses, an InSb detector, CaF_2 beam splitter, and a halogen light source was employed.

Staring materials were aluminosilicate glass chips of composition $(Na_2Si_4O_9)_{90}(Na(NaAl)_4O_9)_{10}$ (denoted NA10) together with solid $Ag_2C_2O_4$ and AgN_3 as sources of CO_2 and N_2, respectively. No reducing agent was added to the starting materials so that all components, including N_2 and CO_2, remain in their oxidized form. The $(Na_2Si_4O_9)_{90}(Na(NaAl)_4O_9)_{1o}$ glass was from the batch originally synthesized by Mysen (2007), but remelted and quenched to glass to be used for starting materials here in order to eliminate incipient crystals and adsorbed and water that may contributed to the sample during its storage. The $Ag_2C_2O_4$ breaks down to metallic Ag and CO_2 gas in between 150° and 200 °C and AgN_3 to metallic Ag and N_2 gas under similar temperature conditions (Boettcher et al. 1973; Roskosz Mysen and Cody, 2006). A few experiments were also conducted with $Ag_2C_2O_4 + H_2O$ only in order to generate reference spectra of volatiles in the COH fluid system.

The sample volume defined by the central hole in the Ir gaskets is about 0.025 mm^3, which poses a major challenge for quantitative addition of individual components to the starting material. To overcome some of the problems posed by these very small samples, a mixture of NA10 + $Ag_2C_2O_4$ + AgN_3 with 8.7 wt% CO_2 and 8.0 wt% N_2 was prepared prior to sample loading. Double-distilled and deionized H_2O was added with the aid of a micro-syringe, but the proportion of H_2O relative to solid materials could not be determined quantitatively because the sample masses are on the order of 0.0x μg. It was, nevertheless attempted to add total solid (NA10 + $Ag_2C_2O_4$ + AgN_3) and liquid H_2O visually estimated to about 1:1 volume proportions.

For both Raman and infrared spectroscopic measurements, the sample was first heated to the highest planned temperature and was kept at this condition for ~ 60 min. This duration is more than sufficient to reach equilibrium for which only several minutes are needed (Horita 1988 2014). Spectroscopic measurements of the sample (fluid, melt, and/or supercritical fluid) together with the ^{13}C diamond were carried out at this highest temperature and pressure condition. The temperature was then decreased at 1 °C/s to the next temperature and pressure condition with the sample remaining in the HADC, and the measurement protocol was repeated. There was some deformation of the Ir gaskets at the highest temperatures of these experiments, which led to sample volume changes. This is why pressure does not decrease monotonously with decreasing temperature (Table 1). Ambient conditions Raman measurements of the ^{13}C diamond were carried before and after a series of high-temperature and high-pressure experiments.

The FTIR measurements were conducted with the same sample contained in the diamond cell as that used for Raman measurements. This sample was subjected to the same temperatures and pressures by using the same protocol as the Raman measurements and was carried out after the Raman measurements were completed. Pressure could not be measured with the diamond shift in the FTIR system. It was assumed, therefore, that for given temperature, the pressure recorded with the ^{13}C diamond in the Raman measurement series was the same during the subsequent FTIR measurements. The validity of this assumption was assessed by monitoring the temperature of gas exsolution from the fluid phase during the Raman and FTIR experiments. Gas exsolution at the same temperature at constant sample volume implies the same pressure at each temperature. In the present experiments, this exsolution temperature was

Table 1 Experimental data

NA10–C–O–H–N		
Temperature, °C*	Pressure, MPa*	Phases
475	63	Melt + fluid
550	262	Melt + fluid
625	361	Melt + fluid
700	489	Melt + fluid
750	679	Melt + fluid
800	643	Single-phase fluid
25	0.1	Glass + gas bubbles
C–O–H		
Temperature, °C*	Pressure, MPa*	Phases
800	865	Fluid
700	267	Fluid
600	132	Fluid
25	0.1	Gas

*Pressure and temperature uncertainties and precision are described in the text

within 10°–15 °C in the Raman and FTIR measurement series. This uncertainty corresponds to a ± 0.02 g/cm^3 density uncertainty for pure H_2O, which for the H_2O density of the experiments reported here corresponds to ± 20 MPa. Equation-of-state data for the fluid mixture are not available, but given that H_2O is a dominant volatile component, ± 20 MPa uncertainty seems reasonable. This conclusion implied a temperature/pressure evolution in the FTIR experiments within error the same as in the Raman measurement series.

The Raman and infrared transmission spectra include contributions from the diamond anvils. This background signal was eliminated in the FTIR spectra by normalizing to those of an empty diamond cell at the same temperature after the sample was removed. For the Raman spectra, the procedure is more complex, and the diamond background was subtracted by using the procedure of Dalou et al. (2015). Briefly, this required recording Raman spectra of the diamond cell away from the sample hole in the Ir gasket but within the same focal plane as the sample measurement at the same temperature and pressure. This spectrum was then subtracted from the sample spectra (melts, fluids, and supercritical fluids), which results in a spectrum without signal contribution from the second-order Raman signal intensity from the diamond cell itself.

The subtraction method used for the Raman spectra could not be used over more than several hundred cm^{-1} frequency range in part because the sensitivity of the CCD detector varies with frequency. Subtraction over wider ranges could, therefore, result in artificial intensity variations. Moreover, in frequency regions with rapid intensity variations, the spectrometer positioning uncertainty (2–3 cm^{-1}) could result in artificial sharp intensity variations. Care was, therefore, exercised to narrow the frequency ranges of Raman spectra to within those of particular interest when conducting the background correction. The infrared spectra suffered from complications resulting from major variations in intensity across the spectra so that in order to obtain reasonable signals from CO_2 and from the overtone/combination bands of water species (see also below) portions of the spectra could not be recorded as the signals commonly saturated the detector. Sample thickness is governed by the gasket thickness and could not, therefore, be varied greatly. It is for this reason that only portions of the infrared spectra are shown.

Results

Experimental conditions are shown in Table 1. In the temperature range from 475 to 750 °C, the samples comprise 30–40 μm diameter melt spheres in a matrix of fluid (Fig. 1). At 800 °C, there is a single fluid phase only. The melt spheres and the fluid matrix could be probed quantitatively with the confocal micro-Raman system because with the ~ 1 μm diameter laser beam the sampling depth is within the range of the sphere diameter or less. In the FTIR spectrometer, however, the minimum aperture is > 30 μm, which means that with the 30–40 μm diameter melt spheres in these experiments, quantitative infrared absorption spectra of melts were not possible because a significant portion of the infrared beam will pass through neighboring fluid. Only infrared absorption spectra of fluid spectra are, therefore, reported.

Infrared absorption spectra

Infrared absorption spectra of fluid in the frequency range of the combination and overtone bands of OH and H_2O (4000–7500 cm^{-1}) can be used to infer changes in total H_2O content as well as proportion of molecular H_2O and OH groups that form bonding with Si^{4+} and Al^{3+} in silicate (e.g., Scholze 1959; Malfait and Xue 2014). The presence of molecular H_2O in fluids (and melts) characteristically results in absorption centered near 5200 cm^{-1}, which has been assigned to a combination band of the H–O–H bending vibration near 1600 cm^{-1} and the OH fundamentals near 3600 cm^{-1} (Fig. 2) (Scholze 1959). The 7200 cm^{-1} band is the first overtone of the 3600 cm^{-1} OH stretch vibrations and has been used to obtain total water content of the sample (Scholze 1959; Dixon et al. 1995; Behrens and Nowak 2003). The 5200 and 7200 cm^{-1} bands broaden significantly with increasing temperature with the broadening of the 7200 cm^{-1} including development of an

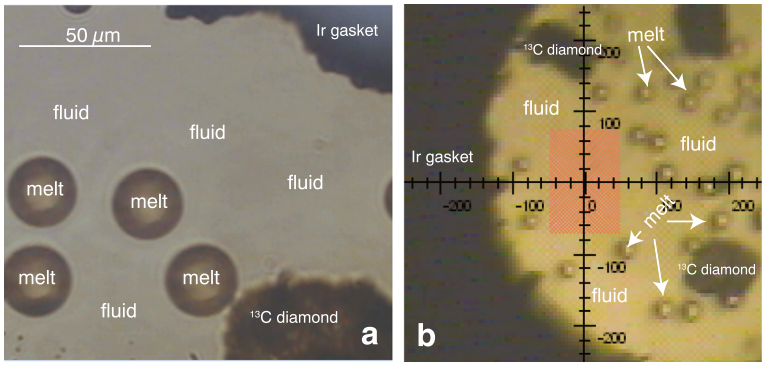

Fig. 1 Microphotograph of samples in the diamond cell at 550 °C and 262 MPa. **a** As viewed through the optical microscope during micro-Raman measurements. The width of the field of view is 200 μm. **b** View of the sample through the optical microscope in the microFTIR system. The numbering on the crosshair indicates μm. The shaded area centered in the cross-hear indicates the position and dimension of the aperture (100 × 150 μm) for fluid examination in this particular experiment

asymmetry toward higher frequency at the highest temperatures.

There is also minor intensity centered near 4500 cm^{-1} at the higher temperatures in the infrared spectra of fluids (see insert in Fig. 2). The 4500 cm^{-1} band is a combination band of the OH fundamentals at 3600 cm^{-1} and vibrations in OH groups attached to Si and Al to form (Si,Al)–OH bond with its main vibrational band between 900 and 950 cm^{-1} (Malfait and Xue 2014). Its integrated intensity increases approximately linearly with increasing temperature to a maximum relative intensity of few percent relative to the 5200 cm^{-1} intensity (Fig. 3). Conversion of this information to concentration requires molar absorption coefficients, which are not available for these fluids. However, if we assume that the 10% difference in these coefficients between the

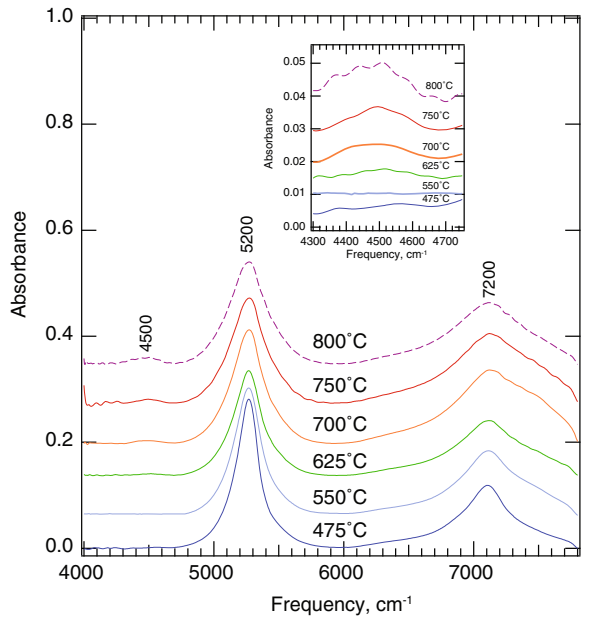

Fig. 2 FTIR spectra of fluid at temperatures indicated. Corresponding pressures can be found in Table 1. The dashed line is the spectrum from a single-phase fluid. Insert shows expanded view of frequency region centered at 4500 cm^{-1}. Note that all spectra are offset for clarity. The 0-intensity line passes through the background at 600 cm^{-1}. In the insert, the 0 line is approximately that near 4300 cm^{-1}

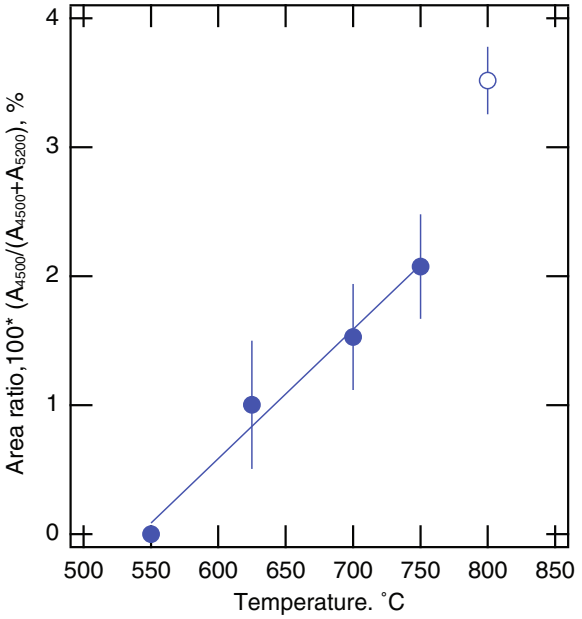

Fig. 3 Relationship between the area of the band centered near 4500 cm^{-1} and that near 5200 cm^{-1} (expressed in percent) from FTIR absorption spectra of fluid. The data point from 800 °C (open circle) is from single-phase fluid. The straight line is a simple linear fit to the data point (not including that from single-phase fluid at 800 °C); area ratio = 0.0100 ± 0.0009–5.4 ± 0.5 T(°C)

4500 and 5200 cm^{-1} absorption from Na_2O–SiO_2 glasses (Yamashita et al. 2008), from the relationship;

$$C_{OH}/C_{H2O} = A_{4500}/\varepsilon_{4500}/(A_{5200}/\varepsilon_{5200}), \quad (1)$$

where C is concentration, A is integrated area, and ε is molar absorption coefficient. The ε_{5200} is about 10% larger than ε_{4500}, which means that the area ratio in Fig. 3 at most underestimates the proportion of OH by about 10%.

Infrared spectroscopy also was employed to probe for species that comprise carbon or nitrogen (CO_2, CO, N_2, N_2O, etc.) or both (e.g., carboxyl groups or CN groups). Among these species, molecular N_2 is infrared inactive, but can be identified, if present, with Raman spectroscopy (see below).

In the spectra of fluids, the only absorption observed is that near 2350 cm^{-1} (Fig. 4), which is assigned as the v_3 antisymmetric stretching in the CO_2 molecule (see Nowak et al. 2003, and references therein). Its integrated intensity is essentially independent of temperature and pressure (see insert A in Fig. 4). Notably, though, the width of this absorption broadens with increasing temperature. It also is asymmetric, wherein a second band could be fitted near 2320 cm^{-1} (see insert B, Fig. 4). This second absorption might exist because there may be variations in the geometry of the CO_2 molecule when dissolved in silicate-saturated C–O–H–N fluid.

Raman spectra

Raman spectra provide information on a range of potentially volatile species as well as silicate species in fluids and melts.

H_2O component

The 3000–4000 cm^{-1} frequency region of the Raman spectra comprises that where signals from the fundamental OH vibrations will occur when water is present in a sample (Walrafen 1967; Holtz et al. 1996). This Raman intensity

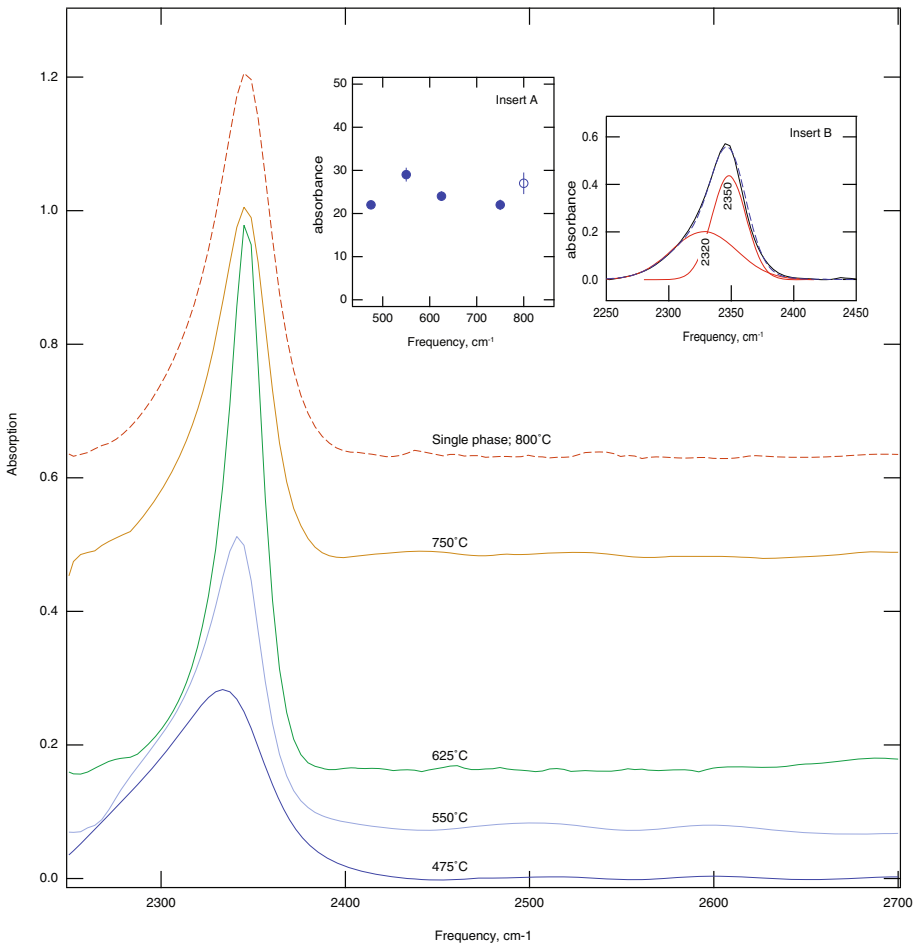

Fig. 4 Infrared absorption spectra of fluids in the spectral region of C–O stretching in CO_2 molecules as a function of temperature and pressure (see Table 1 for pressures). The spectra are offset for clarity. The vertical *line* is the scale bar for the Absorption intensity of the spectra. Inserts A and B show the integrated intensities of the absorption and an example of 2-line curve-fitted infrared spectrum by using Gaussian *line* shape. The spectrum shown was recorded while the sample was at 750 °C. *Dashed line* is from 800 °C where a single fluid phase only exists

includes contributions from both molecular H_2O and structurally bound OH groups.

Sharp, nearly symmetric bands with intensity maxima slightly below 3600 cm^{-1} were recorded in the spectra of all fluids and all melts (Fig. 5a, b). By normalizing the integrated intensities to that in the spectrum of single-phase fluid at 800 °C (diamond in Fig. 5c), we find that this intensity passes through at maximum near 625 °C before decreasing with further temperature increase. The intensities in the spectra of fluid always exceed those of coexisting melt.

The width of the 3600 cm^{-1} Raman bands decreases with increasing temperature (Fig. 5d), which is qualitatively similar to that reported for pure H_2O as well as that of water in silicate-rich hydrous fluids and melts in silicate–H_2O systems (Frantz et al. 1993; Walrafen et al. 1999; Foustoukos and Mysen 2015). This decrease is associated with diminishing asymmetry on the low-frequency-side of the spectrum, a feature that has been ascribed to less influence of hydrogen bonding among water species with increasing temperature (Walrafen et al. 1996, 1999; Foustoukos and Mysen 2012). At all temperatures and pressures, the width of this band in spectra of hydrous melts is greater than in the spectra of silicate-bearing aqueous fluids. This difference reflects either different hydrogen bonding environment in fluids and melts or a broader range of different forms of OH groups might exist in hydrous melts, or both, in hydrous melts as compared with the silicate-bearing C–O–H–N fluids. It is likely that both features contribute. It has been shown, for example, that the enthalpy of hydrogen bond formation of water in silicate melts is less than 50% of the value in aqueous fluids (Mysen 2014). Given the much more silica-rich nature of hydrous melts compared with silicate-saturated C–O–H–N fluids in the temperature and pressure range under a study, it is not

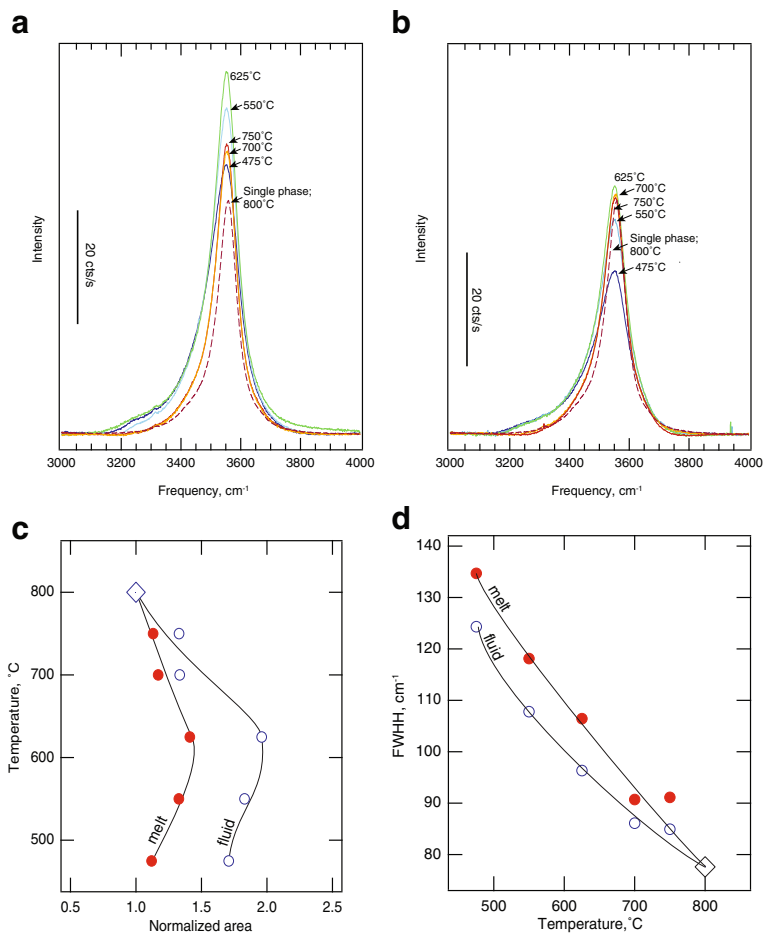

Fig. 5 Raman spectra of coexisting fluid and melt in the high-frequency region of fundamental O–H vibrations. **a** Spectra of fluid at temperatures indicated (corresponding pressures can be found in Table 1). **b** Spectra of coexisting melt (corresponding pressures can be found in Table 1). The spectra are normalized to the same acquisition time with identical focal plane and with otherwise identical instrumental parameters. **c** Normalized areas of coexisting melt and fluid as indicated. **d** Full width at half height, FWHH, from the spectra in Figs. A and B

surprising that a broader range of types of OH formation would be found in water-bearing silicate melts.

Nitrogen component

The most common N-bearing species in the C–O–H–N system could be N_2, N_2O, (N..H)-species, nitride and perhaps CN complexes. Their individual stability depends on bulk composition, temperature, pressure, and redox conditions. There is no evidence in the present spectra for (N..H) complexes (in the 3000–3400 cm^{-1} range; Yeo and Ford, 1994), nitride substitution in SiO_4 tetrahedra (> 1200 cm^{-1}; Sato et al. 1990), and CN-complexes (2000–2200 cm^{-1} frequency range; see, for example, Nakamoto 2009). The lack of Raman signals in the frequency ranges of these possible compounds is consistent with the fact that nitrogen was added as N_2 (from AgN_3 decomposition) and no reducing agent was added to the sample.

Absent a reducing agent, nitrogen in the C–O–H–N system may exist as N_2O, azide (N^{3-}) or as N_2, which are all detectable with Raman spectroscopy. For example, in an experimental study of N-bearing silicate glasses in which Raman and ^{15}N MAS NMR spectroscopies were the structural tools, Roskosz Mysen and Cody (2006) reported that the principal Raman signals from nitrosyl (N_2O) and azide (N≡N) are near 2100 and 2200 cm^1. No Raman signals were detected in this frequency region thus ruling out detectable amounts of such species in either fluid or melt. Whether or not NO_3 groups are formed will be addressed below in the presentation of the low-frequency range comprising vibrations of the silicate network because N–O vibrations occur in the same frequency range (between 1100 and 1200 cm^{-1}; Fung et al. 1994). There is no Raman signal in this frequency range in spectra of fluids. The signal intensity in spectra of melts can be satisfied without resorting to the presence of Raman bands assignable to N–O vibrations in NO_3 groups. This leaves molecular N_2 as the only likely nitrogen species in fluids and melts in the silicate–C–O–H–N system under study here.

The N=N stretch vibrations from molecular N_2 dissolved in silicate melts at high pressure result in Raman bands slightly above 2300 cm^{-1} (Roskosz Mysen and Cody, 2006). The spectra of fluids and melts in the silicate–C–O–H–N system exhibit a single sharp line near 2320 cm^{-1} after the background from second-order Raman peaks in this region from the diamonds in the diamond cell, itself, was subtracted (Fig. 6a, b). The peaks are Gaussian in shape, which is similar to that reported by Roskosz Mysen and Cody (2006) in Raman spectra of N_2-saturated silicate glasses quenched from melts at pressures ≥ 1 GPa. In contrast, gaseous N_2 spectra have sharp Lorentzian peaks. This difference likely reflects some interaction between the N_2 molecules and the hydrous silicate melt matrix in which they are dissolved.

The integrated Raman intensities of these bands, normalized to the same acquisition time and retaining the same focal plane for all measurements show distinctly different abundance behavior with temperature and pressure relative to the value in the spectra of single phase fluid (Fig. 6c). Whereas the normalized abundance in fluid passes through a maximum before decreasing rapidly with increasing temperature and pressure, the normalized abundance of N_2 in the coexisting melt is insensitive to temperature (and pressure).

Carbon component

Carbon speciation in fluids and melts is redox sensitive. Under reducing conditions such as those near the magnetite–wüstite buffer and more reducing, the most common species in silicate–COH system is CH_4 with the dominant Raman signals near 2900–3000 cm^{-1} (Kadik et al. 2004; Mysen et al. 2011; Armstrong et al. 2015). In the absence of hydrogen and under reducing conditions, oxycarbide complexes have been proposed (Libourel et al. 2003; Renlund et al. 1991; Soraru et al. 1995) with the two dominant Raman bands near 1350 and slightly above 1500 cm^{-1}, respectively (Soraru et al. 1995). There is no evidence for any of these species in the Raman spectra of fluids and melts, which is, of course, understandable given the conditions of no reducing agent in samples were carbon was added to the starting materials as CO_2.

Molecular CO_2, CO_3^{2-}, and HCO_3^- groups are the three main C-bearing species under oxidizing conditions. Molecular CO_2 was detected in the infrared absorption spectra of fluid as discussed above (Fig. 4). However, the Fermi diad of molecular CO_2, which at ambient conditions occurs at 1280 and 1380 cm^{-1}, respectively (Rosso and Bodnar 1995; Lamadric et al. 2017), cannot be identified in Raman spectra of the samples contained in diamond cells at high temperatures because the one-phonon Raman shift from the natural diamonds used as anvils in the cell results in a Raman band with intensity that covers those frequency regions. As noted above, infrared spectra could not be obtained from the melt spheres because of their small size. It could not be established, therefore, whether molecular CO_2 also exists in the hydrous silicate melts at high temperature and pressure.

The Raman spectra of fluids and melts may, contain information relevant to possibility of CO_3^{2-} and HCO_3^- groups because of their dominant C–O stretch vibrations near 1070 and 1020 cm^{-1} at ambient temperatures and pressures. The C–O stretch vibration in HCO_3^- is particularly sensitive to temperature and is located near

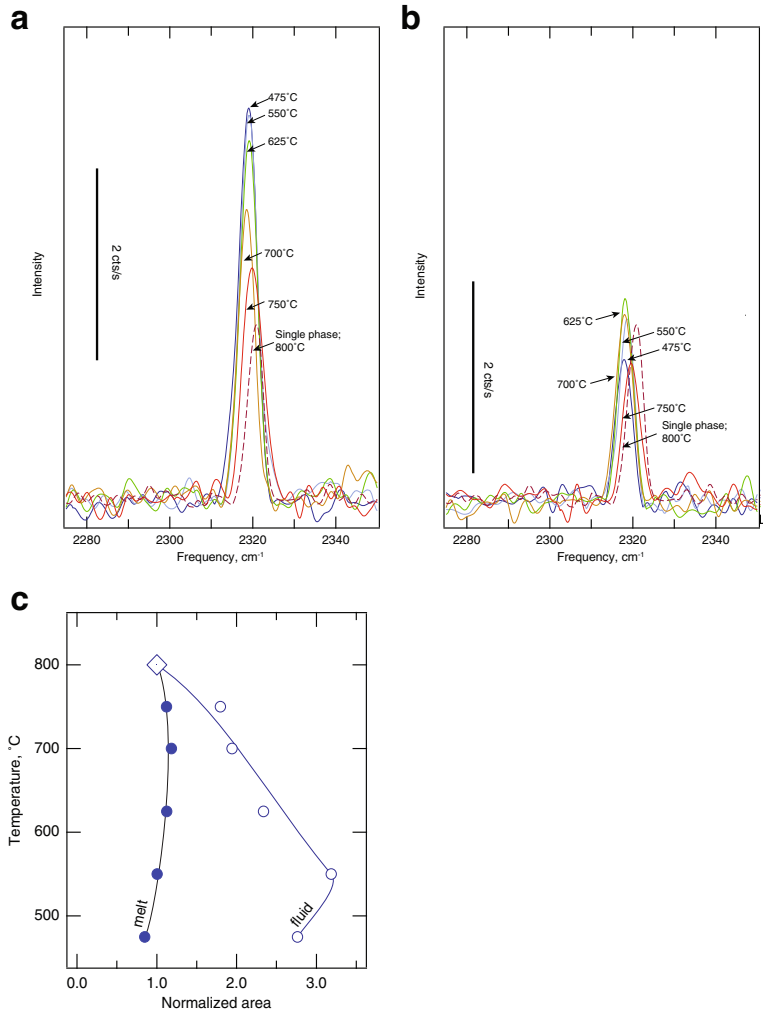

Fig. 6 Raman spectra of coexisting fluid and melt in the high-frequency region of fundamental N=N vibrations. **a** Spectra of fluid at temperatures indicated (corresponding pressures can be found in Table 1). **b** Spectra of coexisting melt (corresponding pressures can be found in Table 1). The spectra are normalized to the same acquisition time with identical focal plane and with otherwise identical instrumental parameters. **c** Areas of coexisting melt and fluid normalized to the area of single phase fluid at 800 °C as a function of temperature and pressure

950 cm^{-1} near 500 °C, for example (Frantz 1998). In simple COH fluids equilibrated at 700 °C and above (without nitrogen and without silicate components), there is evidence for CO_3^{2-} groups from Raman intensity near 1070 cm^{-1} (Fig. 7), which is assigned to C–O stretch vibrations in CO_3^{2-} groups (White 1974; Frantz 1998). A peak that occurs slightly below 1100 cm^{-1} in the spectra of silicate–C–O–H–N melt from 550 °C to the highest temperatures (Fig. 8). The same peak can be detected in spectra of fluids from 550 °C to the highest temperatures. It is assigned to C–O vibrations in CO_3^{2-} groups. Within the scatter of the data, there are no other peaks in this frequency region in the spectra of fluid (Fig. 8a). In the spectra of melts, a second band appears near 1000 cm^{-1} (Fig. 8b), which is assigned to C–OH vibrations in HCO_3^- groups (Frantz 1998). We cannot detect HCO_3^- groups in spectra of fluids. Neither is there any signal above 1100 cm^{-1}, which could be due to N–O vibrations in NO_3 groups in the fluids (Fung et al. 1994).

Absolute concentration of CO_3^{2-} and HCO_3^- groups cannot be obtained from the spectra without assuming that the Raman cross-sections for the two vibrations are similar. It is clear, nevertheless, that in both fluid and coexisting melt, the CO_3^{2-} abundance increase with temperature and pressure until the univariant line that separates melt + fluid from a single fluid is crossed (near 800 °C) (Fig. 9). In this regard, the evolution of the CO_3^{2-} abundance with temperature and pressure resembles those of N_2 and H_2O (Figs. 5c and 6c). There is, however, a difference in that for N_2 and H_2O, these

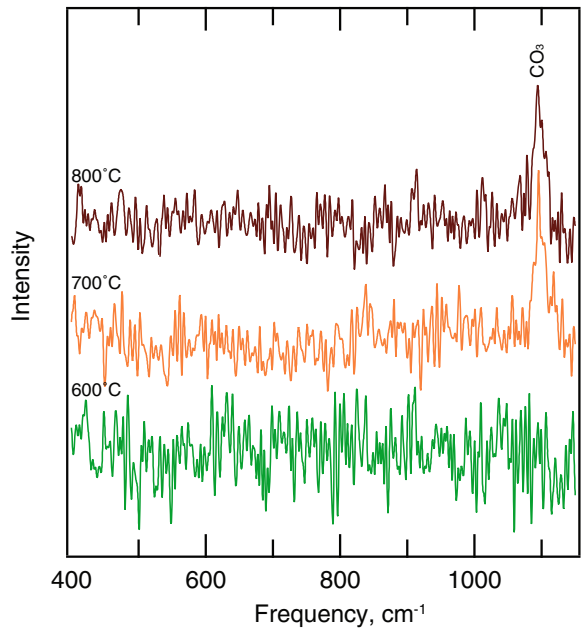

Fig. 7 Raman spectra of COH fluids at 600°, 700°, and 800 °C and corresponding pressures (see Table 1). The peak near 1070 cm^{-1} is assigned to C–O stretch vibrations in CO_3 groups (Frantz et al. 1993) and marked CO_3

components are favored by the fluid, whereas for the CO_3^{2-} groups, these are favored by melt.

Silicate components

Silicate components and their species exist in coexisting silicate melts and C–O–H–N fluid. There are, however, significant differences between the silicate-saturated C–O–H–N fluid and the C–O–H–N-saturated silicate melts as seen, for example, in their significantly different Raman spectra (Fig. 10). In spectra of fluid, the dominant peak is near 780 cm^{-1}, and is assigned to Si–O vibrations in Q^0 species (Zotov and Keppler 2002; Mibe et al. 2008). The spectra of fluid characteristically also comprise a broad band centered near 600 cm^{-1}, with two weaker bands near 810 and 900 cm^{-1}, respectively. The latter two Raman bands are assigned Si–O vibrations in Q^1 and Q^2 species, respectively, whereas that centered near 600 cm^{-1} is an Si–O–Si bending vibration, which requires, therefore, bridging oxygen such as, for example, in Q^1 and Q^2 species (Zotov and Keppler 2002). At frequencies higher than 1000 cm^{-1} in spectra of fluids, there is a weak band near 1070 cm^{-1}, assigned to C–O stretching in CO_3 groups, as discussed under C-bearing species above (see also Fig. 8).

The spectra of coexisting melts differ significantly from those of fluids. They do comprise the 780, 810, and 900 cm^{-1} bands also seen in spectra of fluids, but in addition, there is a band near 1100 cm^{-1} not seen in the fluid spectra. There is also much more intensity at frequencies below 700 cm^{-1} (Fig. 10). The 1100 cm^{-1} is assigned to Si–O vibrations in Q^3 species, whereas the extensive intensity below 700 cm^{-1} is due to bending and rocking motions in polymerized silicate species (McMillan 1984; Neuville et al. 2006; Mibe et al. 2008). The intensity near 500 cm^{-1}, coupled with the shoulder near 550 cm^{-1}, in the spectra of melts suggests that Q^4 species may exist in the C–O–H–N-saturated silicate melts. The 1070 and 1000 cm^{-1} bands, assigned to C–O stretching in CO_3^{2-} and HCO_3^- species, were discussed above (Fig. 8).

The abundance of Q-species and degree of polymerization, NBO/T, of silicate in fluids and melts were derived from the Raman spectra. This was accomplished by assuming that the Raman cross sections of Si–O stretch vibrations in Q^0, Q^1, Q^2, and Q^3 species were the same. The NBO/T can then be calculated from the simple relationship;

$$\mathrm{NBO/T} = \sum_{n=1}^{n=4} (\mathrm{NBO/T})_{Q^n} \bullet X_{Q^n}, \qquad (2)$$

where $(NBO/T)_{Qn}$ is the degree of polymerization of a specific Q-species and X_{Qn} its mol fraction.

The C–O–H–N-saturated melts become increasingly depolymerized (NBO/T increases) with increasing temperature and pressure, whereas that of silicate in the C–O–H–N fluid follows the opposite trend (Fig. 11). These trends qualitatively are the same as those observed in the simpler silicate–H_2O systems (Mysen 2009) and reflect how the H_2O component in silicate–C–O–H–N melts in breaks up the silicate network. The effect becomes more pronounced with increasing temperature and pressure because such increases also most likely are associated with increasing water concentration in the melt. In the C–O–H–N fluids, on the other hand, the silicate solubility increases with increasing temperature and pressure. Increasing silicate concentration in water-bearing fluids results in increasing silicate polymerization (Mysen et al. 2013).

The NBO/T evolution with temperature and pressure reflects the abundance evolution of the Q-species (Fig. 11). For melts, the Q^0 abundance increases with temperature and pressure, that of Q^1 is insensitive, whereas the abundance of more polymerized species, Q^2 and Q^3, decreases with increasing temperature and pressure and, therefore, increasing water content. In other words, the C–O–H–N-saturated melts behave as simpler H_2O-saturated melts, which become increasingly depolymerized with increasing water content (Zotov and Keppler 1998). This behavior contrasts with the silicate dissolved in C–O–H–N fluid, where the abundance of

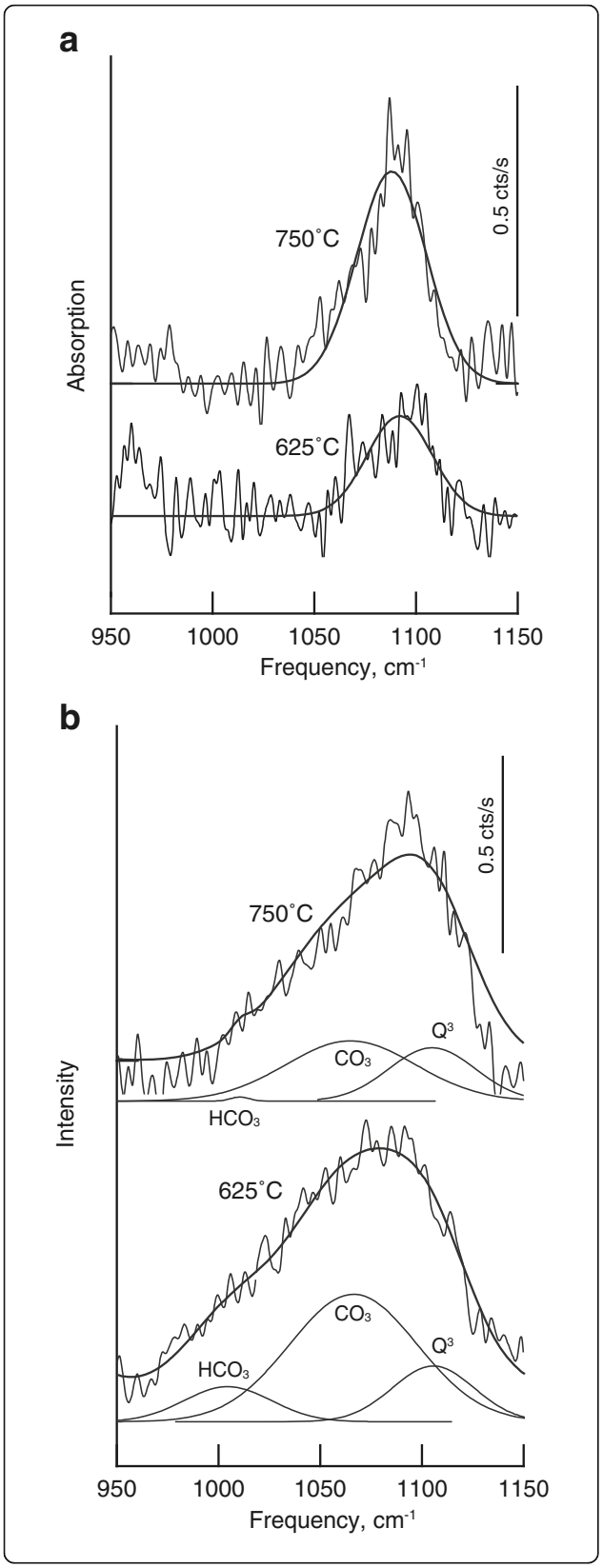

Fig. 8 Example of Raman spectra of silicate–C–O–H–N fluid and melt at 625° and 750 °C, respectively, fitted to Gaussian lines in the 950–1150 cm^{-1} frequency range. **a** Spectra from fluid with a single line assigned to C–O vibrations in CO_3 groups. **b** Spectra from melts where three lines are needed. These are assigned to C–O stretching in HCO_3^- and CO_3^{2-} groups and to Si–O stretching in Q^3 silicate species (see text for discussion on these assignments)

Q^0 species decreases and that of Q^1 increases with increasing temperature and pressure and, therefore, likely total water content (Fig. 11).

Discussion

The solubility mechanisms of volatile species in silicate–C–O–H–N melts qualitatively resemble those in the simpler systems such as silicate–H_2O and silicate–COH. Addition of nitrogen to the system under oxidizing conditions results in formation of molecular N_2, which does not interact chemically with the other volatile components.

Water in the form of molecular H_2O dominates in C–O–H–N fluids with OH groups forming less than 3% of the total water concentration even at the highest temperatures and pressures (Fig. 3). This is less than the proportion of OH groups in pure silicate–H_2O systems at similar temperatures and pressures, where this proportion often exceeds 10% (Mysen 2010). In fact, by using the relationship between proportion of OH in fluid, expressed

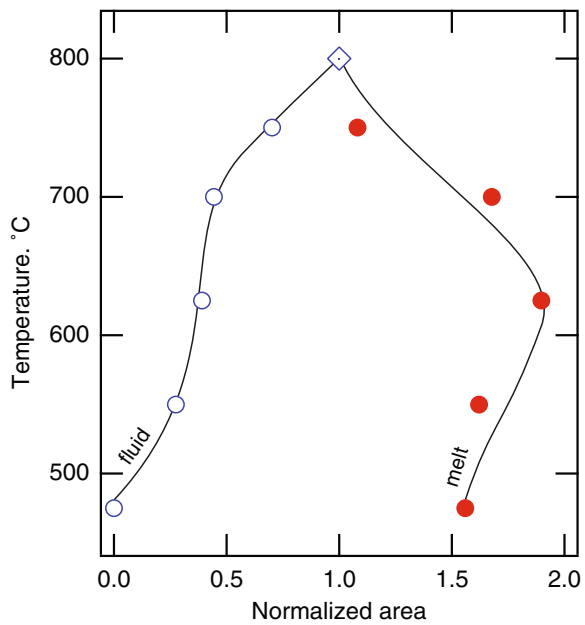

Fig. 9 Evolution of CO_3^2 abundance in coexisting fluid and melt as a function of temperature and pressure with concentration, expressed as area of the ~ 1070 cm^{-1} band normalized to the value for single phase fluid at 800 °C (diamond symbol)

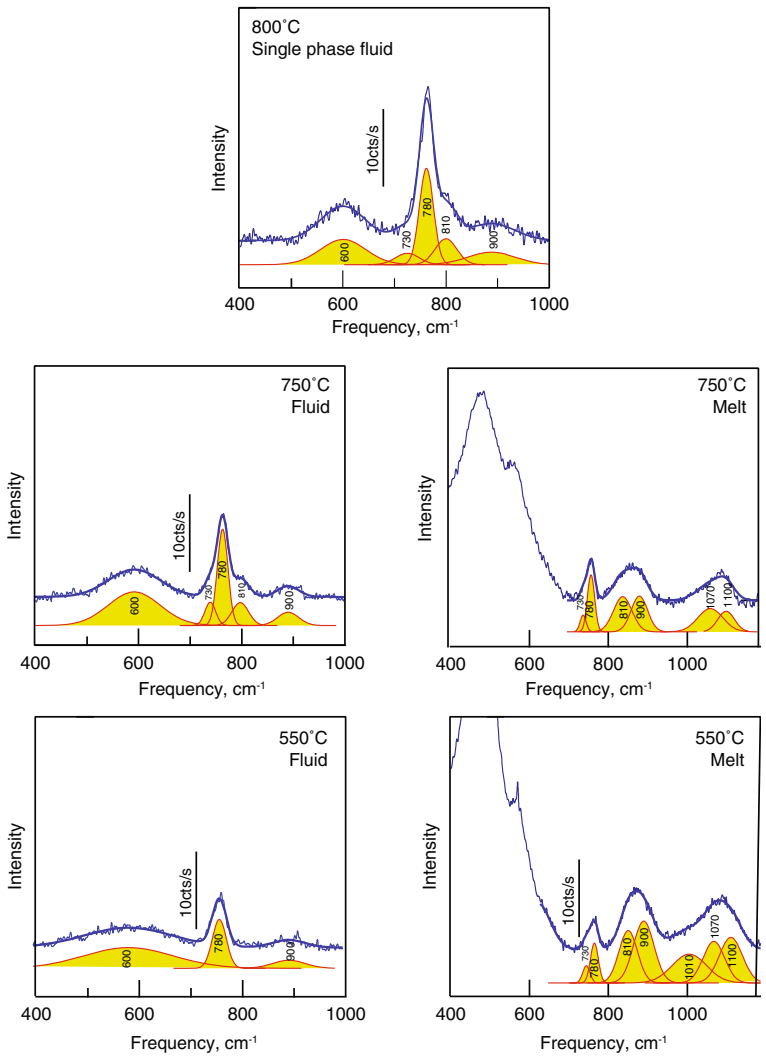

Fig. 10 Examples of Raman spectra of single phase fluid (at 800 °C) and coexisting fluids and melts at temperatures indicated (corresponding pressures in Table 1). Also shown in the spectra are fitted Gaussian lines relevant to structural assignments of silicate and carbonate species. The intensity scale in each spectrum is identical

as $A_{4500}/(A_{4500} + A_{5200})$ from the FTIR data, and fugacity of H_2O for the same silicate composition and pure H_2O (Mysen 2010) (see Fig. 12a), the much lower proportion of OH groups in the C–O–H–N–silicate fluid implies very considerably dilution of water because the f_{H2O} of pure H_2O at the pressures and temperatures of these experiments is in the 200–700 MPa range.

Equivalent OH/H_2O for melt were not obtained for reasons discussed above. However, the overall degree of silicate polymerization as a function of water fugacity, using the NA10–H_2O data from Mysen (2010) for calibration, results in an equivalent f_{H2O} quite similar to that of pure H_2O (Fig. 12b). This observation may suggest that the presence of C and N components in the melt has a much smaller influence on activity composition relations in the (C–O–H–N)-saturated melt than in fluid. This difference reflects the much smaller solubility if silicate components in the fluid than in the melt.

Fluid/melt partition coefficients can be obtained from the ratio of integrated intensities of bands in spectra of coexisting melts and fluids assigned to specific vibrations provided that the instrumental parameters such as acquisition time, slit settings, and focal depth are same during acquisition of both spectra. This can be done because in a ratio of integrated intensities from bands assigned to the same vibration, the remaining variables affecting Raman intensity is temperature, which, of course, is the same for coexisting fluid and melt. Then, the partition coefficient of component, *i*, between fluid and melt, f/m, is;

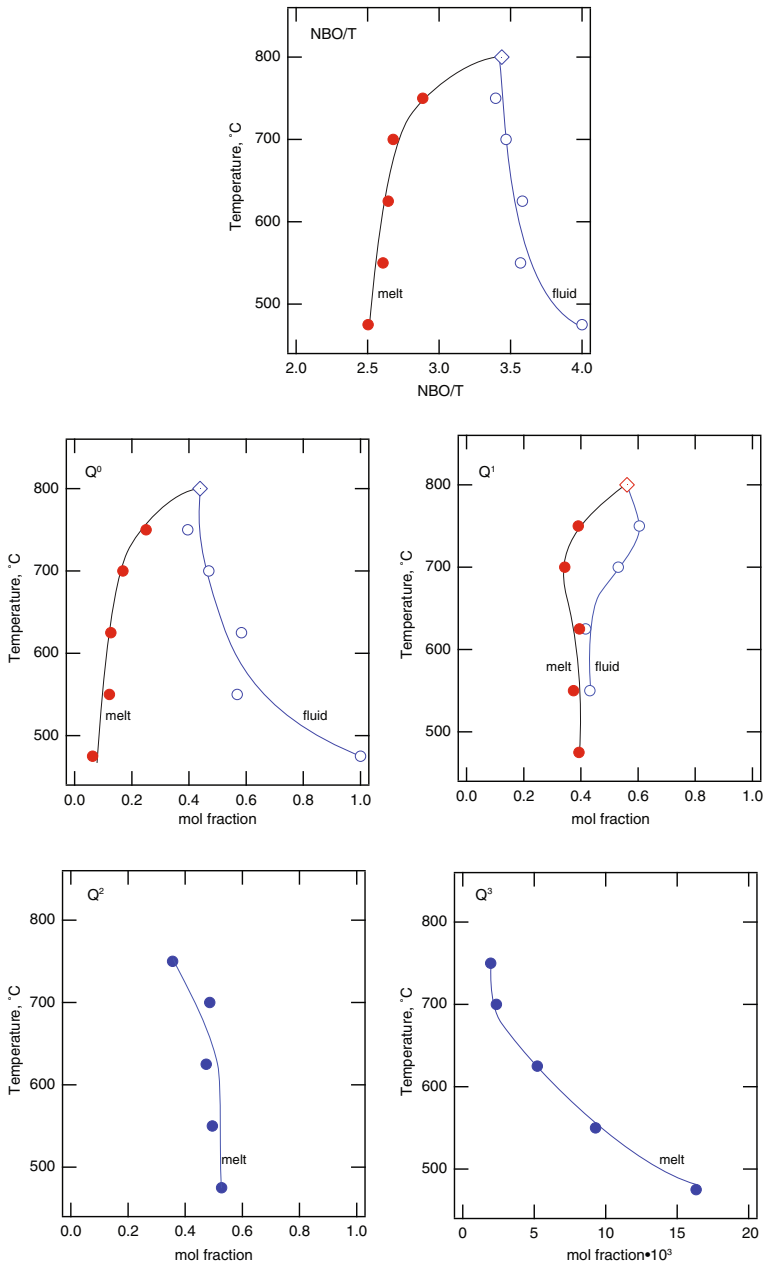

Fig. 11 Evolution of Q-species abundance and bulk NBO/T of melt and coexisting fluid as a function of temperature (and pressure, see Table 1). Note that diamond symbol represents single phase

$$K_i^{f/m} = A_i^f / A_i^m, \quad (3)$$

where A_i^f and A_i^m are the integrated areas from the Raman spectra of a band assigned to a specific type of vibration in component, *i*.

The partition coefficient for total H_2O (which includes all OH-bearing species) can be derived with Eq. (3) from the 3600 cm^{-1} band intensity in spectra of fluids and melts (Fig. 5). This partition coefficient is always greater than unity, which is similar to the partition coefficient in silicate–H_2O systems (Mysen 2013; Webster et al. 2014). From the linear fit to the ln $K_{H2O}^{f/m}$ vs/ 1/T (T is temperature in kelvin), the enthalpy from this partioning is − 6.5 ± 1.5 kJ/mol (Fig. 13), which is quite similar to the results in the simpler silicate–H_2O (Mysen 2013) where ΔH = − 7.6 ± 0.7 kJ/mol. That fact that this ΔH value differs from 0 reflects, most likely, the different extent and type of speciation of H_2O in the coexisting melt and fluid. We should also note that the decreasing partition

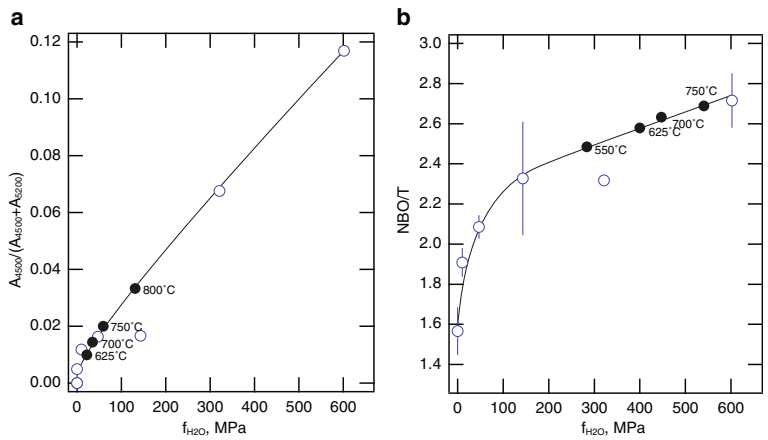

Fig. 12 Relationship between fugacity of H_2O, f_{H2O}, and species abundance. **a** Proportion of OH and molecular H_2O as a function of f_{H2O} in NA10–H_2O fluid from Mysen (2010) (open symbols). Solid symbols plotted onto the line are the date from the current silicate–C–O–H–N fluid. In both cases, the silicate starting composition is NA10. See text for discussion of approximation of OH/(OH + H_2O) ratio with the FTIR absorbance ratio, $A_{4500}/(A_{4500} + A_{5200})$. Silicate polymerization of melt, NBO/T, as a function of f_{H2O} in NA10–H_2O fluid from Mysen (2010) (open symbols). **b** Evolution of NBO/T of the silicate component in the fluid as a function of temperature. Solid symbols plotted onto the line are the data from the current silicate–C–O–H–N fluid. In both cases, the silicate starting composition is NA10

coefficient with increasing temperature actually reflects an increase in pressure as well, which results in increased silicate solubility in fluid and decreased silicate content of hydrous melt (its water content increases). In the isobaric (0.2 GPa) experiments by Webster et al. (2014), no temperature-dependence was observed. That notwithstanding, their fluid/melt partitions fall naturally on the extension of the present data and those of Mysen (2013).

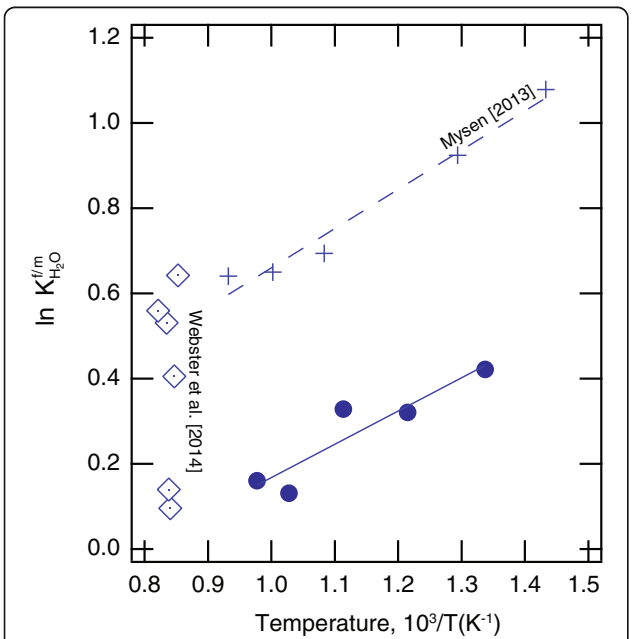

Fig. 13 Partition coefficient between fluid and melt of total H_2O, $K^{f/m}_{H2O}$, as a function of temperature. The least squares straight line fit is, $K^{f/m}_{H2O} = -0.6 \pm 0.2 + 782 \pm 189/T$, $r^2 = 0.85$. Also shown are data from natural samples by Webster et al. (2014) and from experimental data in silicate–H_2O from Mysen (2014). The least squares fit through the data of Mysen (2013) yields the expression, $K^{f/m}_{H2O} = -0.3 \pm 0.1 + 782 \pm 920/T$, $r^2 = 0.97$

For carbon species in melts and fluids in the silicate–C–O–H–N system, there are also similarities between the data and those in the simpler silicate–COH system (Mysen 2015a). However, there also are differences. For example, in the silicate-saturated C–O–H–N fluid, we have evidence only of molecular CO_2 and CO_3^{2} groups, whereas in the silicate–COH system, Mysen (2015a) also observed evidence of HCO_3^{-} groups in the fluid. This difference implies that in the C–O–H–N fluids studied here, the simple carbonate equilibrium;

$$2HCO_3^{-} = 2CO_3^{2} + 2H^{+}, \quad (4)$$

is shifted further to the left than was the case in the COH fluids studied by Mysen (2015a). The implication is that the C–O–H–N fluids examined here are more alkaline that those examined by Mysen (2015a).

For C–O–H–N-saturated melts, on the other hand, there is spectroscopic evidence for both CO_3^{2} and HCO_3^{-} groups. No evidence could be found for molecular CO_2 in the spectra of melt. A simple solution mechanism involving an equilibrium between CO_3^{2} and HCO_3^{-} is (Mysen 2015a):

$$2CO_3^{2-} + H_2O + 2Q^{n} = 2HCO_3^{-} + 2Q^{n-1}. \quad (5)$$

In Eq. (5), Q^{n}, and Q^{n-1}, are silicate species with, respectively, n and n–1 bridging oxygen. The CO_3^{2-}/HCO_3^{-} abundance ratio in melts increases with increasing temperature with $\Delta H = 114 \pm 22$ kJ/mol (Fig. 14). The

HCO_3^- abundance in melt diminishes rapidly with increasing temperature and can barely be observed at 750 °C and cannot be seen in spectra of single phase fluids at 800 °C. In comparison, in the N-free system silicate–COH, also examined in the hydrothermal diamond anvil cell with similar protocol, the CO_3/HCO_3^- ratio was determined for the fluid to be considerably less sensitive to temperature with a $\Delta H = 17 \pm 3$ kJ/mol (Fig. 14).

The fluid/melt partition coefficients for CO_3^{2-} groups are in the range of ~ 0.2 to ~ 0.7 as a function of increasing temperature and pressure with an enthalpy of 52 ± 14 kJ/mol (Fig. 15). These values fall in the range reported by Webster et al. (2014) and Mysen (2015b) even though the compositions in those experiments differed significantly from those of the present compositions.

Even though nitrogen exists in coexisting fluid and melt only as molecular N_2, there are differences in the interaction between the C–O–H–N fluid matrix in fluid and N_2 and silicate matrix in melts and N_2. This difference results in distinctly temperature-dependent N_2 partition coefficients with an enthalpy change (– 20 ± 4 kJ/mol; see Fig. 16) that is considerably greater than the – 6.5 ± 1.5 kJ/mol observed for H_2O partitioning between fluid and melt, for example (Fig. 13). The nitrogen partition coefficients also are more than 20% greater (and increasing with decreasing temperature) than for H_2O. It would seem, therefore, that the activity-composition relations of N_2 in melts, and perhaps fluids, differ from those of H_2O. This difference likely is because H_2O may dissolve both as molecular H_2O and as OH groups forming bonding the silicate network, whereas there is no evidence that N_2 behaves in such a manner.

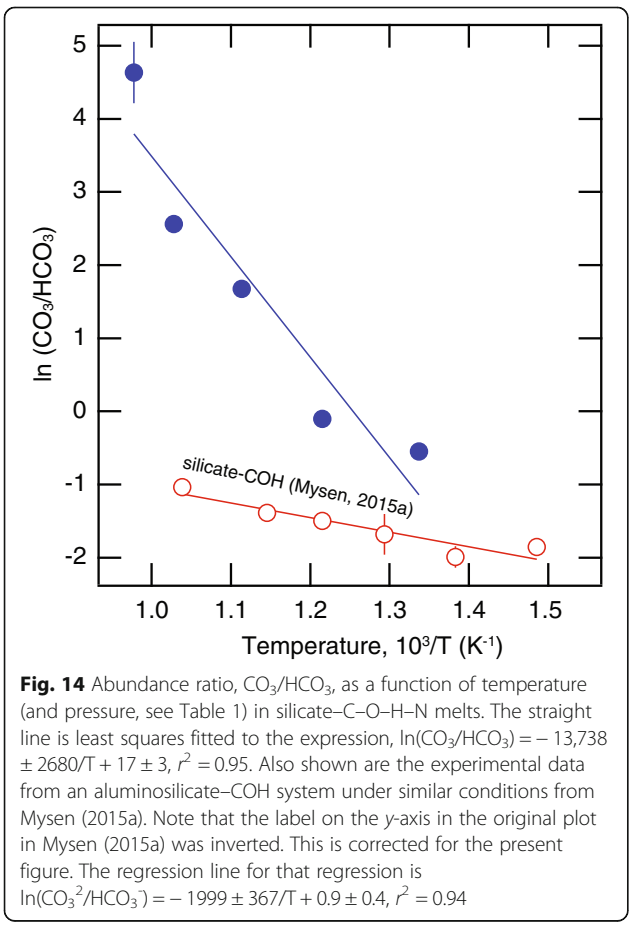

Fig. 14 Abundance ratio, CO_3/HCO_3, as a function of temperature (and pressure, see Table 1) in silicate–C–O–H–N melts. The straight line is least squares fitted to the expression, $\ln(CO_3/HCO_3) = -13{,}738 \pm 2680/T + 17 \pm 3$, $r^2 = 0.95$. Also shown are the experimental data from an aluminosilicate–COH system under similar conditions from Mysen (2015a). Note that the label on the *y*-axis in the original plot in Mysen (2015a) was inverted. This is corrected for the present figure. The regression line for that regression is $\ln(CO_3^{2-}/HCO_3^-) = -1999 \pm 367/T + 0.9 \pm 0.4$, $r^2 = 0.94$

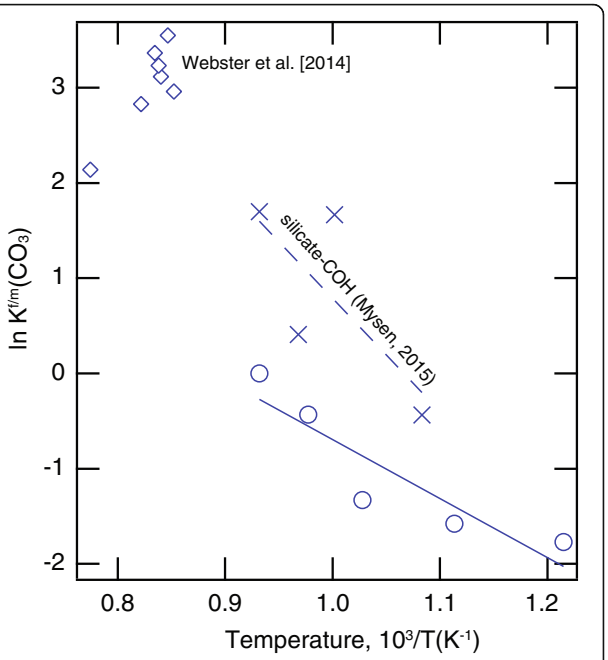

Fig. 15 Partition coefficient of CO_3^{2-} groups between coexisting fluid and melt as a function of temperature. Partition coefficients were determined as discussed under Eq. (1) in the text. The straight line fit by least squares regression yields; $\ln K = 6 \pm 2 – 6203 \pm 1620/T$, $r^2 = 0.83$. Also shown are data from Mysen (2015a) from a silicate–COH system, also under oxidizing conditions. The dashed lines represents a least squares linear fit through those data, with the expression $\ln(CO_3^{2-}/HCO_3^-) = -11{,}893 \pm 7610/T + 13 \pm 8$, $r^2 = 0.74$ as well as data from Webster et al. (2014) using natural silicate melts and COH fluids that also contains halogens and sulfur

Conclusions

It follows from the observations here and in the literature (Mysen et al. 2008; Li and Keppler 2014) that where redox conditions in the Earth are more oxidizing than those defined by the NNO–H_2O and FMQ–H_2O buffer nitrogen released into fluid or melt will most likely exist as molecular N_2. In other words, there is no evidence to indicate chemical interaction between N_2 and other volatile and silicate species under such circumstances.

Redox conditions similar to these are those observed in subduction zones, for example (Wood et al. 1990; Cottrell and Kelley 2011). Under these conditions,

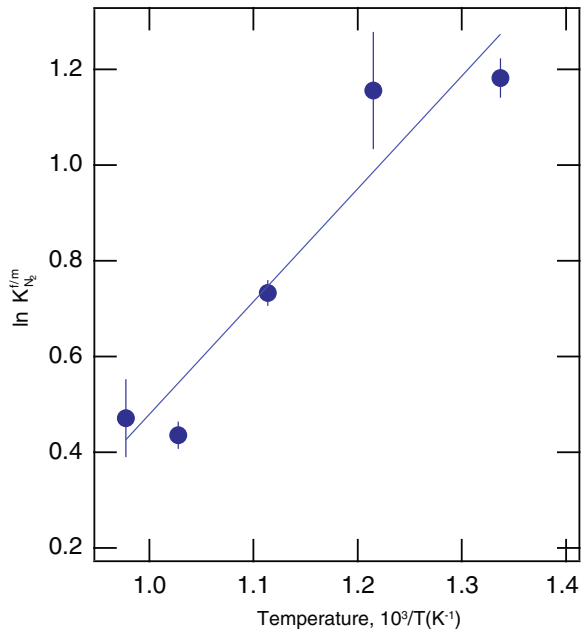

Fig. 16 Partition coefficient between fluid and melt of N_2, $K_{N2}^{f/m}$, as a function of temperature. The least squares straight line fit is, $K_{H2O}^{f/m} = -1.9 \pm 0.5 + 2356 \pm 450/T$, $r^2 = 0.90$

nitrogen effectively serves as a diluent of the volatile species. Dilution is indicated, for example, by the low OH/H_2O ratio of the C–O–H–N fluid (Fig. 12), which indicates lesser water activity than in silicate–H_2O fluids. This much lower OH/H_2O ratio probably this because silicate solubility in C–O–H–N fluids must be considerably less than in the absence of N_2. This follows from simple relationships of the form;

$$Si^{4+} + H_2O = Si(OH)^{3+} + H^+, \quad (6)$$

Where Si^{4+} is a proxy for silicate components and $Si(OH)^{3+}$ a proxy for hydroxylated silicate. This means that as the activity of silicate decreases, the equation shifts to the left thus reducing the proportion of OH groups in the system,

It also appears, therefore, that a decrease of silicate activity in solution in the fluid resulting from the dilution of H_2O by other fluid components enhances fluid alkalinity. This feature, in turn, may alter the solubility of pH-dependent minor and trace elements in the fluid (e.g., high field strength cations; see Ayers et al. 2012) and, therefore result in different element patterns resulting from C–O–H–N fluid release than from release of fluids without N_2, where the silicate solubility is greater and the fluid likely is less alkaline. These features are, of course, also dependent on redox conditions because under reducing conditions nitrogen may form ammonia or ammine-type complexes (Mysen and Fogel, 2010; Li and Keppler 2014), which results in significant changes the behavior of nitrogen in both fluids and melt.

It appears that C–O–H–N-saturated melts are less sensitive to the presence of N_2 than C–O–H–N fluids as both the degree of melt polymerization, NBO/T, and silicate species abundance, appear insensitive to the existence of molecular N_2. However, as is the case for fluids, when magmatic activity occurs where conditions are sufficiently reducing to nitrogen to ammonia and ammine groups (somewhere near the hydrogen fugacity defined by the magnetitie–wüstite–H_2O redox buffer; see Mysen et al. 2008), this may change because the solubility of reduced nitrogen in silicate melts is much greater than oxidized nitrogen. Furthermore, the solution mechanism of reduced nitrogen as NH-complexes resembles that of dissolved H_2O (Mysen et al. 2014). Thus, nitrogen in magmatic liquids under such reducing conditions would tend to enhance melt properties that are sensitive to melt polymerization.

Acknowledgements
Instrument, electronics and library support was provided by Geophysical Laboratory technical staff. Their support is gratefully acknowledged.

Funding
This research was supported in by grant EAR1212854 from the National Science Foundation.

Availability of data and materials
All original data are available from the author on request.

Author's contributions
All research reported in this report was carried out by the author.

Competing interests
The author declares that he has no competing interests.

Publisher's Note

Received: 19 September 2017 Accepted: 15 December 2017
Published online: 24 January 2018

References

Agee CR (2008) Static compression of silicate melt and the effect of water on planetary differentiation. Earth Planet Sci Lett 265,641–654.
Armstrong LS, Hirschmann MM, Stanley BD, Falksen EG, Jacobsen SD (2015) Speciation and solubility of reduced C-O-H-N volatiles in mafic melt: implications for volcanism atmospheric evolution and deep volatile cycles in the terrestrial planets. Geochim Cosmochim Acta 171:283–302
Ayers JC, Zhang L, Luo Y, Peters TJ (2012) Zircon solubility in alkaline aqueous fluids at upper crustal conditions. Geochim Cosmochim Acta 96:18–28
Bassett WA, Wu T-C, Cho I-M, Haselton T, Frantz JD, Mysen BO, Schiferl D (1996) The hydrothermal diamond anvil cell (DAC) and its applications. In: Dyar MD, McCammon CA, Schaefer M (eds) Mineral spectroscopy: a tribute to Roger G burns. The Geochemical Society, Houston, pp 261–272
Bebout GE (2007) Metamorphic chemical geodynamics of subduction zones. Earth Planet Sci Lett 260:373–393
Behrens H, Nowak M (2003) Quantification of H_2O speciation in silicate glasses and melts by IR spectroscopy - in situ versus quench techniques. Phase Transit 76:45–61

Boettcher AL, Mysen BO, Allen JC (1973) Techniques for the control of water fugacity and oxygen fugacity for experimentation in solid-media high-pressure apparatus. J Geophys Res 78:5898–5902

Carmichael ISE, Ghiorso MS (1990) Controls on oxidation-reduction relations in magmas. In: Nicholls J, Russell JK (eds) Modern methods of igneous petrology: understanding magmatic processes. The Mineralogical Society of America, Washington DC, pp 191–212

Cottrell E, Kelley KA (2011) The oxidation state of Fe in MORB glasses and the oxygen fugacity of the upper mantle. Earth Planet Sci Lett 308:1–13

Dalou C, Le Losq C, Mysen BO (2015) In situ study of the fractionation of hydrogen isotopes between aluminosilicate melts and coexisting aqueous fluids at high pressure and high temperature-implications for the delta D in magmatic processes. Earth Planet Sci Lett 426:158–166

Deines P (2002) The carbon isotope geochemistry of mantle xenoliths. Earth-Sci Rev 58:247–278.

Dingwell DB, Webb SL (1990) Relaxation in silicate melts. Eur J Mneral 2:427–449

Dixon JE, Stolper EM, Holloway JR (1995) An experimental study of water and carbon dioxide solubilities in mid-ocean ridge basaltic liquids part 1 calibration and solubility models. J Petrol 36:1607–1631

Fisher TP, Hilton DR, Zimmer M, Shaw AM, Sharp ZD, Walker JA (2002) Subduction and recycling if nitrogen along the central American margin. Science 297:1154–1157

Foustoukos D, Mysen BO (2015) The structure of water-saturated carbonate melts. Am Mineral 100:35–46

Foustoukos DI, Mysen BO (2012) D/H isotopic fractionation in the H_2-H_2O system at supercritical water conditions: composition and hydrogen bonding effects. Geochim Cosmochim Acta 86:88–102

Frantz G (1998) Raman spectra of potassium carbonate and bicarbonate aqueous fluids at elevated temperatures and pressures: comparison with theoretical simulations. Chem Geol 152:211–225

Frantz JD, Dubessy J, Mysen B (1993) An optical cell for Raman spectroscopic studies of supercritical fluids and its applications to the study of water to 500°Cand 2000 bar. Chem Geol 106:9–26

Frost DJ, McCammon CA (2008) The redox state of the Earth's mantle. Annu Rev Earth Planet Sci 36:389–384

Fung KH, Imre DG, Tang IN (1994) Detection limits for sulfates and nitrates in aerosol particles by Raman spectroscopy. J Aerosol Sci 25:479–485

Holtz F, Beny JM, Mysen BO, Pichavant M (1996) High-temperature Raman spectroscopy of silicate and aluminosilicate hydrous glasses: implications for water speciation. Chem Geol 128:25–39

Horita J (1988) Hydrogen isotope analyses of natural waters using an H_2-water equilibration method: a special implication to brines. Chem Geol 72:89–94

Horita J (2014) Oxygen and carbon isotope fractionation in the system dolomite–water–CO_2 to elevated temperatures. Geochim Cosmochim Acta 129:111–124

Jambon A (1994) Earth degassing and large-scale geochemical cycling of volatile elements. In: Carroll MR, Holloway JR (eds) Volatiles in Magmas. Mineralogical Society of America, Washington DC, pp 479–517

Javoy M (1997) The major volatile elements of the earth: their origin, behaviour and fate. Geophys Res Lett 24:177–180

Kadik A, Pineau F, Litvin Y, Jendrzejewski N, Martinez I, Javoy M (2004) Formation of carbon and hydrogen species in magmas at low oxygen fugacity. J Petrol 45:1297–1310

Kadik AA, Koltashev VV, Kryukova EB, Plotnichenko VG, Tsekhonya TI, Kononkova NN (2015) Solubility of nitrogen carbon and hydrogen in FeO-Na_2O-Al_2O_3-SiO_2 melt and liquid iron alloy: influence of oxygen fugacity. Geochem Int 53:849–868

Kadik AA, Kurovskaya NA, Ignat'ev YA, Kononkova NN, Koltashev VV, Plotnichenko VG (2010) Influence of oxygen fugacity on the solubility of carbon and hydrogen in FeO-Na_2O-SiO_2-Al_2O_3 melts in equilibrium with liquid iron at 15 GPa and 1400 degrees. Geochem Int 48:953–960

Kasting JF, Eggler DH, Raeburn SP (1993) Mantle redox evolution and the oxidation state of the Archean atmosphere. J Gol 101:245–257

Kessel R, Ulmer P, Pettke T, Schmidt MW, Thompson AB (2004) A novel approach to determine high-pressure high-temperature fluid and melt compositions using diamond-trap experiments. Am Mineral 89:1078–1086

Lamadric HM, More LR, Moncada D, Rimstidt RJ, Burruss RC, Bodnar RJ (2017) Reassessment of the Raman CO_2 densimeter. Chem Geol 450:210–222

Li Y, Keppler H (2014) Nitrogen speciation in mantle and crustal fluids. Geochim Cosmochim Acta 129:13–32

Liang Q, Yan C-S, Meng Y, Lai J, Krasnicki A, Mao H-K, Hemley R (2009) Recent advances in high-growth rate single-crystal CVD diamonds. Diamonds Rel Mater 18:698–703

Libourel G, Marty B, Humbert F (2003) Nitrogen solubility in basaltic melt part I effect of oxygen fugacity. Geochim Cosmochim Acta 67:4123–4136

Malfait WJ, Xue X (2014) Hydroxyl speciation in felsic magmas. Geochim Cosmochim Acta 140:606–620

Marty B (1995) Nitrogen content of the mantle inferred from N_2-Ar correlation in oceanic basalt. Nature 377:326–329

McMillan P (1984) Structural studies of silicate glasses and melts-applications and limitations of Raman spectroscopy. Am Mineral 69:622–644

Mibe K, Chou I.-M., Bassett W A (2008) In situ Raman spectroscopic investigation of the structure of subduction-zone fluids. J Geophys Res 113. https://doi.org/10.1029/2007JB005179.

Moynihan CT, Macedo PB, Montrose CJ, Gupta PK, De Bolt MA, Dill JF, Wilder JA (1976) Structural relaxation in vitreous materials. Ann N Y Acad Sci 279:15–35

Mysen B (2010) Structure of H_2O-saturated peralkaline aluminosilicate melt and coexisting aluminosilicate-saturated aqueous fluid determined in-situ to 800 C and 800 MPa. Geochim Cosmochim Acta 74:4123–4139

Mysen B (2013) Effects of fluid and melt density and structure on high-pressure and high-temperature experimental studies of hydrogen isotope partitioning between coexisting melt and aqueous fluid. Am Mineral 98:1754–1764

Mysen B (2015a) Carbon speciation in silicate-C-O-H melt and fluid as a function of redox conditions: an experimental study in situ to 1.7 GPa and 900 degrees. Am Mineral 100:872–882

Mysen B (2015b) Hydrogen isotope fractionation and redox-controlled solution mechanisms in silicate-COH melt plus fluid systems. J Geophys Res 120:7440–7459

Mysen BO (2007) The solution behavior of H_2O in peralkaline aluminosilicate melts at high pressure with implications for properties of hydrous melts. Geochim Cosmochim Acta 71:1820–1834

Mysen BO (2009) Solution mechanisms of silicate in aqueous fluid and H_2O in coexisting silicate melts determined in-situ at high pressure and high temperature. Geochim Cosmochim Acta 73:5748–5763

Mysen BO (2014) Water-melt interaction in hydrous magmatic systems at high temperature and pressure. Prog Earth Planet Sci 1. doi:https://doi.org/10.1186/2197-4284-1-4

Mysen BO, Armstrong L (2002) Solubility behavior of alkali aluminosilicate components in aqueous fluids and silicate melts at high pressure and temperature. Geochim Cosmochim Acta 66:2287–2298

Mysen BO, Fogel ML (2010a) Nitrogen and hydrogen isotope compositions and solubility in silicate melts in equilibrium with reduced (N+H)-bearing fluids at high pressure and temperature: effects of melt structure. Am Mineral 95:987–999

Mysen BO, Kumamoto K, Cody GD, Fogel ML (2011) Solubility and solution mechanisms of C-O-H volatiles in silicate melt with variable redox conditions and melt composition at upper mantle temperatures and pressures. Geochim Cosmochim Acta 75:6183–6199

Mysen BO, Lucier A, Cody GD (2003) The structural behavior of Al^{3+} in peralkaline melts and glasses in the system Na_2O-Al_2O_3-SiO_2. Am Mineral 88:1668–1678

Mysen BO, Mibe K, Chou I-M, Bassett WA (2013) Structure and equilibria among silicate species in aqueous fluids in the upper mantle: experimental SiO_2-H_2O and MgO-SiO_2-H_2O data recorded in-situ to 900°C and 54 GPa. J Geophys Res 118:6076–6085

Mysen BO, Yamashita S (2010) Speciation of reduced C-O-H volatiles in coexisting fluids and silicate melts determined in-situ to similar to 1.4 GPa and 800 degrees. Geochim Cosmochim Acta 74:4577–4588

Mysen BO, Yamashita S, Chertkova N (2008) Solubility and solution mechanisms of NOH volatiles in silicate melts at high pressure and temperature-amine groups and hydrogen fugacity. Am Mineral 93:1760–1770

Nakamoto K (2009) Infrared and Raman spectra of inorganic and organic coordination compounds part B: applications in coordination Crganometallic and Cioorganic chemistry chapter 1. John Wiley, sons, Hoboken NJ

Neuville DR, Cormier L, Massiot D (2006) Al coordination and speciation in calcium aluminosilicate glasses: effects of composition determined by ^{27}Al MQ-MAS NMR and Raman spectroscopy. Chem Geol 229:173–185

Newton RC, Manning CE (2005) Solubility of anhydrite CaSO4 in NaCl–H_2O solutions at high pressures and temperatures: applications to fluid–rock interaction. J Petrol 46:701–716

Newton RC, Manning CE (2006) Solubilities of corundum wollastonite and quartz in H_2O-NaCl solutions at 800°C and 10 kbar: interaction of simple minerals

with brines at high pressure and temperature. Geochim Cosmochim Acta 70:5571–5582
Ni HW, Keppler H (2013) Carbon in silicate melts. Rev Mineral Geochem Carbon in Earth 75:251–287
Nowak M, Behrens H (1995) The speciation of water in haplogranitic glasses and melts by in-situ near-infrared spectroscopy. Geochim Cosmochim Acta 59:3445–3450
Nowak M, Porbatzki D, Spickenbom K, Diedrich O (2003) Carbon dioxide speciation in silicate melts: a restart. Earth Planet Sci Lett 207:131–139
Renlund GM, Prochazka S, Doremus RH (1991) Silicon oxycarbide glasses 2 structure and properties. J Mater Res 6:2723–2734
Richet P, Bottinga Y (1986) Thermochemical properties of silicate glasses and liquids: a review. Rev Geophys 24:1–25
Richet P, Neuville DR, Courtial P, Tequi C (1992) Thermodynamic and rheological properties of silicate melts. In: Anonymous (ed) 29th international geological congress; abstracts, vol 29, p 540
Roskosz Mysen BO, Cody GD (2006) Dual speciation of nitrogen in silicate melts at high pressure and temperature: an experimental study. Geochim Cosmochim Acta 70:2902–2918
Rosso KM, Bodnar RJ (1995) Microthermometric and Raman spectroscopic detection limits of CO_2 in fluid inclusions and the Raman spectroscopic characterization of CO_2. Geochim Cosmochim Acta 59:3961–3975
Sato R, Bolvin J, McMillan PF (1990) Synthesis and characterization of a SiAlON glass. J Amer Ceram Soc 73:2494–2497
Schiferl D, Nicol M, Zaug JM, Sharma SK, Cooney TF, Wang S-Y, Fleischer JF (1997) The diamond $^{13}C/^{12}C$ isotope Raman pressure sensor system for high temperature/pressure diamond-anvil cells with reactive samples. J Appl Phys 82:3256–3265
Schmidt MW, Poli S (2003) Generation of mobile components during subduction of oceanic crust. Treatise on Geochemistry: Elsevier:567–591
Scholze H (1959) Über die quantitative IR-spektroskopische Wasser-Bestimmung in Silicaten. Angew Chem 71:678
Soraru GD, D'Andrea G, Compostrini R (1995) Structural characterization and high-temperature behavior of silicon oxycarbide glasses prepared from sol-gel precursors containing Si-H bonds. J Amer Ceram Soc 78:379–387
Stebbins JF (1988) Effects of temperature and composition on silicate glass structure and dynamics: Si-29 NMR results. J Non-Cryst Solids 106:359–369
Tolstikhin IN, Marty B (1998) The evolution of terrestrial volatiles: a view from helium argon and nitrogen isotope modeling. Chem Geol 147:27–52
Walrafen GE (1967) Raman spectral studies of HDO in H_2O. J Chem Phys 48:244–251
Walrafen GE, Yang W-H, Chu YC (1999) Raman spectra from saturated water vapor to the supercritical fluid. J Phys Chem B 103:1332–1338
Walrafen GE, Yang WH, Chu YC, Hokmabadi MS (1996) Raman OD-stretching overtone spectra from liquid D_2O between 22 and 152 degrees C. J Phys Chem 100:1381–1139
Webster JD, Goldoff B, Sintoni MF, Shimizu N, De Vivo B (2014) C-O-H-Cl-S-F volatile Solubilities partitioning and mixing in Phonolitic-Trachytic melts and aqueous-carbonic vapor +/− saline liquid at 200 MPa. J Petrol 55:2217–2247
White WB (1974) The carbonate minerals. In: Farmer VC (ed) Infrared spectra of minerals. Mineralogical Society of London, London, p Ch 12
Wood BJ, Bryndzia LT, Johnson KE (1990) Mantle oxidation state and its relationship to tectonic environment and fluid speciation. Science 248:337–345
Wu L, Yang D-B, Xie H-S, Li F-F, Hu B, Yu Y, Gao C-X (2014) Pressure-induced elastic and structural changes in hydrous basalt glasses: the effect of H_2O on the gravitational stability of basalt melts at the base of the upper mantle. Earth Planet Sci Lett 406:165–173
Yamada A, Inoue T, Urakawa S, Funakoshi K-I, Nobumasa F, Kikegawa T, Irifune T (2011) In situ X-ray diffraction study on pressure-induced structural changes in hydrous forsterite and enstatite melts. Earth Planet Sci Lett 308:115–123
Yamashita S, Behrens H, Schmidt BC, Dupree R (2008) Water speciation in sodium silicate glasses based on NIR and NMR spectroscopy. Chem Geol 256:231–241
Yeo GA, Ford TA (1994) Ab initio molecular orbital calculations of the energetic structural vibrational and electronic properties of some hydrogen bonded complexes of water ammonia and hydroxylamine. Spectrochim Acta 50A:5–18
Zhang Y-G, Frantz JD (2000) Enstatite-forsterite-water equilibria at elevated temperatures and pressures. Am Mineral 85:918–925
Zotov N, Keppler H (1998) The influence of water on the structure of hydrous sodium tetrasilicate glasses. Am Mineral 83:823–834
Zotov N, Keppler H (2002) Silica speciation in aqueous fluids at high pressures and high temperatures. Chem Geol 184:71–82